ChemComm

COMMUNICATION

View Article Online
View Journal | View Issue

Cite this: *Chem. Commun.*, 2025, **61**, 12590

Received 1st July 2025,
Accepted 17th July 2025

DOI: 10.1039/d5cc03713a

rsc.li/chemcomm

Asymmetric linker generates intrinsically disordered metal–organic framework with local MOF-74 structure†

Bhavish Dinakar, ‡*[a] Julius J. Oppenheim, ‡*[b] Marco Vandone,[bc] Juan F. Torres,[b] Andrei Iliescu,[b] Zhentao Yang,[b] Yuriy Román-Leshkov[a] and Mircea Dincă[b]

Here, we report an intrinsically disordered MOF in the MOF-74 family, Mg_{2-x}(as-dobpdc) (as-dobpdc^{4-} = 3′,4-dioxidobiphenyl-3,4′-dicarboxylate). Despite the absence of crystallinity, this material exhibits local ordering consistent with that of its crystalline isomers, maintains porosity, and exhibits a high density of open metal sites.

Metal–organic frameworks (MOFs) are typically valued for their combination of crystallinity, porosity, and tunability.[1] However, amorphous MOFs can retain local order while introducing advantages, such as broader distribution of active sites types, reduced thermal conductivity, and emergent modes of tunability *via* control over the type of disorder.[2,3] Conventional amorphization strategies rely on external stimuli including pressure, temperature, stress, electrical discharge, or fast precipitation.[4–10] Recently, amorphous MOFs have been accessed directly using low symmetry organic linkers.[11]

Here, we employed a symmetry-reduction strategy to access an amorphous isomer within the MOF-74 structural family. In the benzene-based series, there are two isomers: 2,5-dihydroxybenzene-1,4-dicarboxylic acid and 4,6-dihydroxybenzene-1,3-dicarboxylic acid. These combine with transition metals to form the crystalline MOFs M_2(dobdc) (also known as MOF-74, CPO-27, and M_2(dhbdc)) and M_2(*m*-dobdc), respectively.[12,13] For the biphenyl-derived series, two isomers have been reported: M_2(pc-dobpdc) (also referred to as IRMOF-74-II; pc-dobpdc^{4-} = 3,3′-dioxidobiphenyl-4,4′-dicarboxylate) and M_2(mc-dobpdc) (mc-dobpdc^{4-} = 4,4′-dioxidobiphenyl-3,3′-dicarboxylate, where pc- and mc- refer to *para-* and *meta*-carboxylate substitution, respectively).[14,15] Here, we investigate a third isomer, 3′,4-dioxidobiphenyl-3,4′-dicarboxylate (as-dobpdc^{4-}), which yields a new porous material, Mg_{2-x}(as-dobpdc), where "as" refers to asymmetric substitution. Even though the secondary building units for Mg_2(mc-dobpdc) and Mg_2(pc-dobpdc) have similar connectivity, differences in bond angles introduce geometric frustration in Mg_{2-x}(as-dobpdc), leading to amorphization and loss of long-range order (Fig. 1). Despite this, Mg_{2-x}(as-dobpdc) retains porosity and has pore size distributions and local order (as probed by X-ray pair distribution function) comparable to those of its crystalline counterparts. Additionally, Mg_{2-x}(as-dobpdc) retains open metal sites, with ∼0.9 sites per Mg.

Synthetic conditions for Mg_{2-x}(as-dobpdc) were adapted from previously reported procedures for Mg_2(mc-dobpdc) and Mg_2(pc-dobpdc). Most synthesis attempts yielded either amorphous solids or metal salts, as confirmed by powder X-ray diffraction (PXRD) (Fig. S20–S22, ESI†). However, an optimized synthesis condition using $Mg(NO_3)_2{\cdot}6H_2O$ and H_4(as-dobpdc) in a 1 : 1 (vol) mixture of *N*,*N*-diethylformamide and methanol at 120 °C in a silanized vial produced a pale yellow solid, denoted Mg_{2-x}(as-dobpdc). PXRD of this material exhibited broad, low-intensity diffuse peaks centered at 2θ values of ∼5° and ∼8° (Fig. 2), indicative of a largely amorphous material with some local order. These reflections align with the characteristic {100} and {110}/{$\bar{1}\bar{1}$0} peaks of crystalline Mg_2(mc-dobpdc) (space group $P3_121$; CCDC 1827449) and the {110} and {300} reflections of Mg_2(pc-dobpdc) (space group $R\bar{3}$; CCDC 841642), suggesting structural similarity at the local scale. A model structure of an idealized Mg_2(as-dobpdc) framework (Fig. S18, ESI†) also shows simulated PXRD peaks at these positions (Fig. S19, ESI†), providing a plausible depiction of local connectivity. The PXRD of Mg_{2-x}(as-dobpdc) remained unchanged after washing with *N*,*N*-dimethylformamide (DMF) and methanol, or after activation under dynamic vacuum at 180 °C (Fig. S23, ESI†). Thermogravimetric analysis (TGA) of Mg_{2-x}(as-dobpdc) did not show significant mass loss of material until temperatures >200 °C (Fig. S37, ESI†).

[a] *Department of Chemical Engineering, Massachusetts Institute of Technology, 77 Massachusetts Ave, Cambridge MA 02139, USA. E-mail: bdinakar@mit.edu*
[b] *Department of Chemistry, Massachusetts Institute of Technology, 77 Massachusetts Ave, Cambridge MA 02139, USA. E-mail: joppenhe@mit.edu*
[c] *Dipartimento di Chimica & UdR INSTM di Milano, Università degli Studi di Milano, 20133 Milan, Italy*

† Electronic supplementary information (ESI) available: Full characterization and experimental methods. See DOI: https://doi.org/10.1039/d5cc03713a

‡ These authors contributed equally.

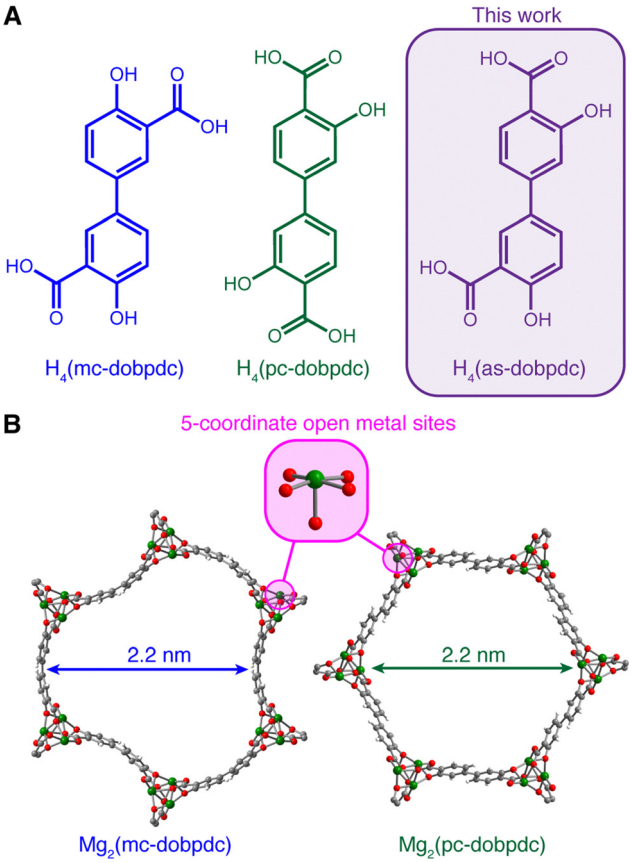

Fig. 1 (A) Comparison of H_4(mc-dobpdc) and H_4(pc-dobpdc) linkers used to form previously reported MOF-74-type structures with H_4(as-dobpdc) linker used in this work. (B) Depiction of structures of Mg_2(mc-dobpdc) and Mg_2(pc-dobpdc) which both contain hexagon-shaped pores and coordinatively unsaturated metal sites.

We next attempted to determine the composition of Mg_{2-x}(as-dobpdc). ^{1}H NMR analysis of digested activated Mg_{2-x}(as-dobpdc) (using D_2SO_4 and d_6-DMSO, in accordance with procedures used for other MOF-74 materials[16–18]) showed the presence of H_4(as-dobpdc) and residual DMF in a ratio of ~0.45 DMF per H_4(as-dobpdc). This residual solvent could not be removed under the activation conditions used. Thermogravimetric analysis (TGA) was employed to quantify the inorganic content: the sample was first activated at 180 °C, then oxidized in air at 800 °C (Fig. S38, ESI†), yielding MgO as the final residue (Fig. S40, ESI†). Combining TGA and NMR data yields a formula of $Mg_{1.9}H_{0.2}$(as-dobpdc)[DMF]$_{0.45}$. A comparable empirical formula, $Mg_{1.76}H_{0.48}$(as-dobpdc)[$DMF_{0.45}$][$(H_2O)_{0.69}$], was independently derived from elemental analysis by fitting C, H, N, and Mg content (Section S10, ESI†). Both formulas (Mg_{2-x}(as-dobpdc) with x = 0.1–0.25) suggest that although the ratio of Mg to linker is close to the ideal value of 2, there is an excess of linker relative to Mg that is consistent with the low crystallinity of the material.

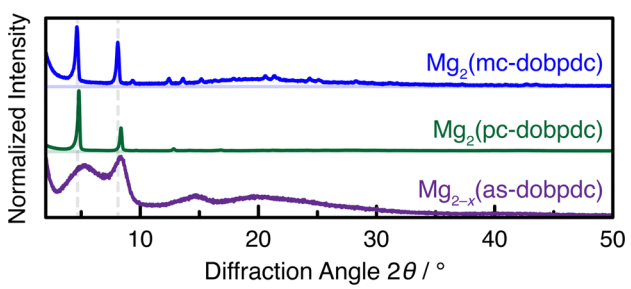

Fig. 2 Powder X-ray diffractograms (Cu Kα radiation, λ = 1.5418 Å) of Mg_2(mc-dobpdc), Mg_2(pc-dobpdc), and Mg_{2-x}(as-dobpdc) obtained by dropcasting the solids from the synthesis suspension. Dashed lines at ~5° and ~8° are shown to guide the eye.

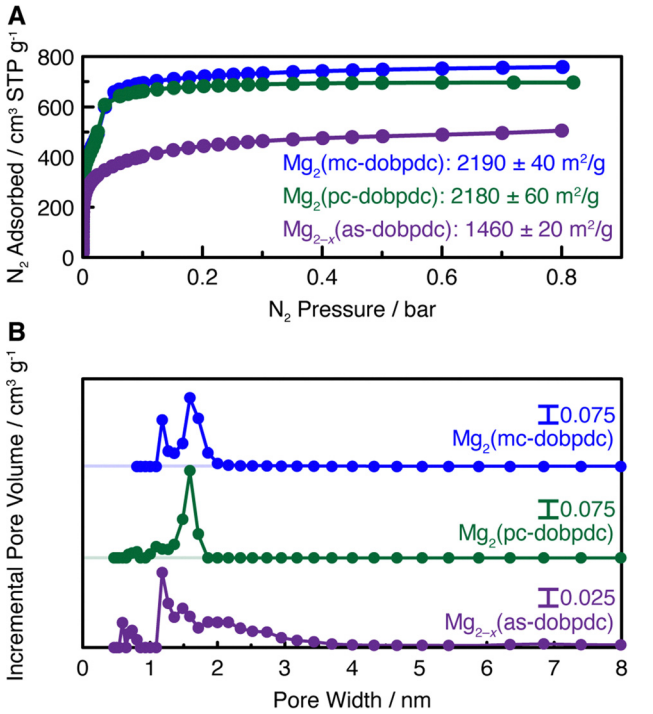

Fig. 3 (A) 77 K N_2 adsorption isotherms of activated Mg_2(mc-dobpdc), Mg_2(pc-dobpdc), and Mg_{2-x}(as-dobpdc) with fitted BET surface areas. (B) Pore size distributions obtained from fitting the N_2 adsorption isotherms.

To understand the structure of Mg_{2-x}(as-dobpdc), we collected N_2 adsorption isotherms at 77 K and compared with those of Mg_2(mc-dobpdc) and Mg_2(pc-dobpdc) (Fig. 3A). The Brunauer–Emmett–Teller (BET) surface areas were 2190 ± 40 m^2 g^{-1} for Mg_2(mc-dobpdc), 2180 ± 60 m^2 g^{-1} for Mg_2(pc-dobpdc), and 1460 ± 20 m^2 g^{-1} for Mg_{2-x}(as-dobpdc). Although the BET surface area for Mg_{2-x}(as-dobpdc) is lower than that of the crystalline analogues, the material still displays remarkable porosity despite its largely amorphous character.

The pore size distributions were calculated with the "N_2 – DFT Model" as implemented in Micromeritics software (Fig. 3B). The fitted distributions for Mg_2(mc-dobpdc) and Mg_2(pc-dobpdc) predominantly show micropores, consistent with the expected crystallographic structures. Interestingly, the fitted distribution for Mg_{2-x}(as-dobpdc) shows significant microporosity, with most pores falling below 4 nm in width. Although the calculated values are approximate, owing to the use of an idealized slit-pore model, they clearly show that

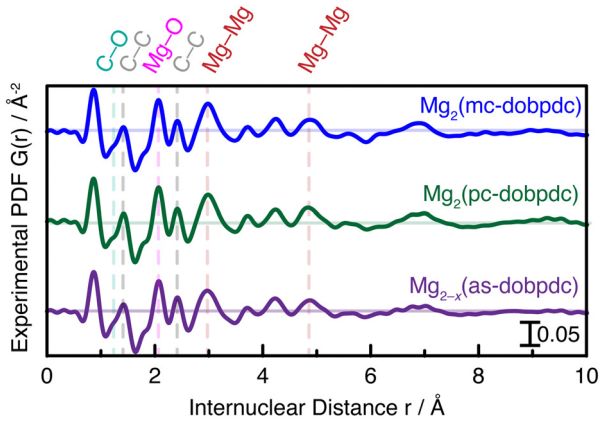

Fig. 4 Pair distribution functions (PDFs) of Mg_2(mc-dobpdc), Mg_2(pc-dobpdc), and Mg_{2-x}(as-dobpdc). Labelled vertical dashed lines correspond to distances between particular element pairs.

Mg_{2-x}(as-dobpdc) contains a large fraction of micropores, similar to the other analogues.

To further probe the local structure, we performed X-ray pair distribution function (PDF) analysis to determine interatomic distances in the three materials. While PDF does not provide an exact global structural model for Mg_{2-x}(as-dobpdc); comparison with the crystalline analogues provides information for the local structure and the ordering length scaling. Interestingly, all three PDFs are almost identical for internuclear distances <10 Å (Fig. 4), suggesting their local structures are preserved despite differences in long-range order. At larger distances (10–30 Å), the PDF intensity for Mg_{2-x}(as-dobpdc) decays faster (Fig. S43, ESI†), as expected from the lower crystallinity.

Using previously obtained crystal structures for Zn_2(mc-dobpdc) and Zn_2(pc-dobpdc) (isostructural to the Mg analogues), we simulated PDFs in order to assign specific element pairs to the peaks in the experimental PDF (Fig. S42, ESI†). From this analysis, we found that in addition to C–O and C–C pairs occurring at similar internuclear distances (expected as they originate solely from the framework linker), we also found that Mg–O and Mg–Mg pairs occur at similar internuclear distances in all three frameworks, providing further evidence that the local metal–ligand geometry is preserved in Mg_{2-x}(as-dobpdc), despite its lack of long-range order.

As an additional test of local structure, we sought to determine if any of the Mg atoms in Mg_{2-x}(as-dobpdc) contained open metal sites. As all of the Mg sites formed in Mg_2(mc-dobpdc) and Mg_2(pc-dobpdc) are coordinatively unsaturated, we hypothesized that if Mg_{2-x}(as-dobpdc) had a similar local structure to the other analogues, then it should also contain a high density of open metal sites. Previous studies have demonstrated that these open sites can be functionalized with diamines for CO_2 capture, providing a strategy for quantifying their accessibility.[16–18] Using established protocols, we appended 2-methyl-1,2-diaminopropane (dmen) to Mg_{2-x}(as-dobpdc), targeting a 1 : 1 dmen : Mg stoichiometry as observed in the crystalline analogues.[16–18] To quantify the Mg-bound dmen, we activated dmen–Mg_{2-x}(as-dobpdc) at 130 °C under N_2 *via* TGA to remove physisorbed dmen, followed by oxidation to MgO by heating to 800 °C under air, where the dmen content could be calculated by the difference in inorganic : organic ratios before and after appending dmen to the framework. We also used the same activation procedure *via* TGA on a different batch of dmen–Mg_{2-x}(as-dobpdc), after which we performed ^{1}H NMR after digestion to quantify the ratio of diamine to linker. This ^{1}H NMR did not contain DMF, indicating that dmen displaced DMF coordinated to the Mg sites during appending. Both the TGA method ($\sim$0.93 dmen : Mg, Fig. S46, ESI†) and the ^{1}H NMR method ($\sim$0.9 dmen : Mg, Fig. S47, ESI†) provided similar dmen : Mg ratios of $\sim$90%, suggesting that most Mg sites in the framework strongly bind dmen, and were likely coordinatively unsaturated. Of these open sites, elemental analyses suggest that $\sim$80% can be accessed after activation, with the rest remaining bound to DMF, which can be displaced by dmen.

To probe if the local environment of these coordinatively unsaturated metal sites was similar in the three frameworks, we performed transmission Fourier transform infrared spectroscopy (IR) using acetone as a probe molecule. Specifically, the C=O stretching frequency, ν(C=O), of acetone is a well-established reporter of Lewis acidity, with red-shifted frequencies corresponding to stronger Lewis acids.[19] In addition, this vibrational frequency is sensitive to local electric fields, which can stabilize the C–O bond dipole and similarly lead to red shifts.[20] Therefore, we hypothesized that if the ν(C=O) frequencies of Mg-bound acetone were significantly different between the three frameworks, it could indicate either a difference in Lewis acidity of the Mg or a difference in the local environment generating an electric field; either case would reflect changes in the local structure.

We collected IR spectra by first activating pelletized samples under flowing N_2 at 130 °C, followed by cooling to 30 °C under the same atmosphere. The gas stream was then switched to N_2 saturated with acetone vapor to fill the framework pores, and subsequently returned to pure N_2 to monitor desorption. Spectra were recorded every 2 minutes relative to the acetone-free baseline at 30 °C to isolate features associated with strongly bound acetone, which is expected to desorb more slowly than the physisorbed species. For both Mg_2(mc-dobpdc) (Fig. S53, ESI†) and Mg_2(pc-dobpdc) (Fig. 5A), desorption spectra show a strongly bound peak in the ν(C=O) region at $\sim$1727 cm^{-1}, which we attribute to Mg-bound acetone, in addition to a quickly desorbing peak at $\sim$1710 cm^{-1}, which we attribute to intraporous acetone. For Mg_{2-x}(as-dobpdc), we observe a similar strongly bound acetone feature at $\sim$1725 cm^{-1}, suggesting that the local environment of the Mg-bound acetone is similar in all three frameworks. We note that there is some baseline fluctuation for Mg_{2-x}(as-dobpdc) between 1640–1480 cm^{-1}, due to perturbation of the ν(C=O) stretching frequency from residual DMF interacting with acetone as well as the DMF vibrational modes (Fig. S52, ESI†).

Here, we have demonstrated that the amorphous MOF Mg_{2-x}(as-dobpdc) has little to no global translational symmetry, yet preserves porosity. The framework has similar pore size

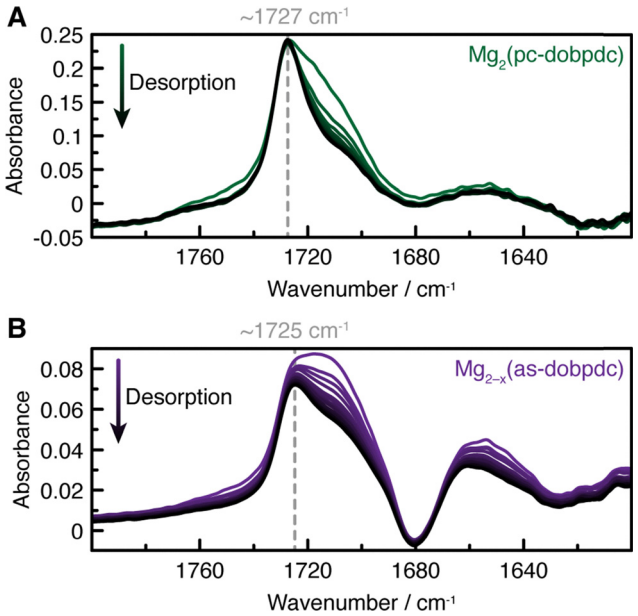

Fig. 5 Transmission-mode Fourier transform infrared spectra of acetone desorption from (A) Mg_2(pc-dobpdc) and (B) Mg_{2-x}(as-dobpdc), background-subtracted from the bare framework spectra. The peaks marked by dashed gray lines (~1727 cm^{-1} and ~1725 cm^{-1}) are assigned to the C═O mode of acetone bound to the Mg sites.

distribution and local order to both Mg_2(mc-dobpdc) and Mg_2(pc-dobpdc). Moreover, it maintains a high degree (~0.9 sites per Mg) of open metal sites, suggesting that even without crystallinity, the framework may possess similar functionality. We expect that the Mg deficiency, as compared to the crystalline isomorphs, will result in defects that have potential applications in catalysis and gas sorption/separation. Similarly, the difference in pore size distribution could potentially be exploited for adsorbing larger molecules than the ones accessible for crystalline isomorphs. While no crystalline phase of Mg_{2-x}(as-dobpdc) has yet been isolated, we cannot rule out the possibility that appropriate synthetic conditions may yield a crystalline phase. We envision that this strategy of linker symmetry reduction might lead to a new class of amorphous MOFs that may have emergent functionality.

This work was supported by the Department of Energy (DOE), Office of Basic Energy Sciences (DE-SC0016214) and National Science Foundation (DMR-2105495). B. D. was supported by the National Science Foundation Graduate Research Fellowship Program (2141064). NMR spectroscopy was performed at the MIT DCIF. Scanning electron microscopy was performed through MIT.nano. This work used beamline 28-ID-1 of the National Synchrotron Light Source II, a DOE Office of Science User Facility, operated by Brookhaven National Laboratory under Contract No. DE-SC0012704. The authors thank Dr. Gihan Kwon for help with PDF measurement.

Conflicts of interest

There are no conflicts to declare.

Data availability

The data supporting this article have been included as part of the ESI.†

Notes and references

1 S. R. Batten, N. R. Champness, X.-M. Chen, J. Garcia-Martinez, S. Kitagawa, L. Öhrström, M. O'Keeffe, M. P. Suh and J. Reedijk, *Pure Appl. Chem.*, 2013, **85**, 1715–1724.
2 T. D. Bennett and A. K. Cheetham, *Acc. Chem. Res.*, 2014, **47**, 1555–1562.
3 J. Fonseca, T. Gong, L. Jiao and H.-L. Jiang, *J. Mater. Chem. A*, 2021, **9**, 10562–10611.
4 W. M. W. Winters, C. Zhou, J. Hou, M. Diaz-Lopez, T. D. Bennett and Y. Yue, *Chem. Mater.*, 2024, **36**, 8400–8411.
5 Y. Feng, M.-Y. Zou, H.-C. Hu, W.-H. Li, S.-L. Cai, W.-G. Zhang and S.-R. Zheng, *Chem. Commun.*, 2022, **58**, 5013–5016.
6 N. L. Baun, S. S. Mortensen, H. Bordallo, K. Jensen and A. Sapnik, *ChemRxiv*, 2025, preprint, DOI: 10.26434/chemrxiv-2025-psg4n.
7 H. Wang, Y. Liu, L. Li, J. Zhang, M. Luo, Z. Sun, Y. Xiao, X. Zhai, L. Wu, H. Zhang, B. Ye, C. Yang, X. Zhang and M. Zhou, *Angew. Chem., Int. Ed.*, 2025, **137**(28), e202506960.
8 R. Zacharia, D. Cossement, L. Lafi and R. Chahine, *J. Mater. Chem.*, 2010, **20**, 2145–2151.
9 Y. Zhou and C. Liu, *Plasma Chem. Plasma Process.*, 2011, **31**, 499–506.
10 Y. H. Hu and L. Zhang, *Phys. Rev. B: Condens Matter Mater. Phys.*, 2010, **81**, 174103.
11 E. G. Meekel, E. M. Schmidt, L. J. Cameron, A. D. Dharma, H. J. Windsor, S. G. Duyker, A. Minelli, T. Pope, G. O. Lepore, B. Slater, C. J. Kepert and A. L. Goodwin, *Science*, 2023, **379**, 357–361.
12 N. L. Rosi, J. Kim, M. Eddaoudi, B. Chen, M. O'Keeffe and O. M. Yaghi, *J. Am. Chem. Soc.*, 2005, **127**, 1504–1518.
13 M. T. Kapelewski, S. J. Geier, M. R. Hudson, D. Stück, J. A. Mason, J. N. Nelson, D. J. Xiao, Z. Hulvey, E. Gilmour, S. A. FitzGerald, M. Head-Gordon, C. M. Brown and J. R. Long, *J. Am. Chem. Soc.*, 2014, **136**, 12119–12129.
14 T. M. McDonald, W. R. Lee, J. A. Mason, B. M. Wiers, C. S. Hong and J. R. Long, *J. Am. Chem. Soc.*, 2012, **134**, 7056–7065.
15 H. Deng, S. Grunder, K. E. Cordova, C. Valente, H. Furukawa, M. Hmadeh, F. Gándara, A. C. Whalley, Z. Liu, S. Asahina, H. Kazumori, M. O'Keeffe, O. Terasaki, J. F. Stoddart and O. M. Yaghi, *Science*, 2012, **336**, 1018–1023.
16 R. L. Siegelman, T. M. McDonald, M. I. Gonzalez, J. D. Martell, P. J. Milner, J. A. Mason, A. H. Berger, A. S. Bhown and J. R. Long, *J. Am. Chem. Soc.*, 2017, **139**, 10526–10538.
17 P. J. Milner, J. D. Martell, R. L. Siegelman, D. Gygi, S. C. Weston and J. R. Long, *Chem. Sci.*, 2017, **9**, 160–174.
18 B. Dinakar, A. C. Forse, H. Z. H. Jiang, Z. Zhu, J.-H. Lee, E. J. Kim, S. T. Parker, C. J. Pollak, R. L. Siegelman, P. J. Milner, J. A. Reimer and J. R. Long, *J. Am. Chem. Soc.*, 2021, **143**, 15258–15270.
19 K. Shimizu, T. Higuchi, E. Takasugi, T. Hatamachi, T. Kodama and A. Satsuma, *J. Mol. Catal. A: Chem.*, 2008, **284**, 89–96.
20 S. D. E. Fried, C. Zheng, Y. Mao, T. E. Markland and S. G. Boxer, *J. Phys. Chem. B*, 2022, **126**, 5876–5886.